Prediction of Gas Sorption Kinetics for Porous Media Using MRI

Matthew J. Watt-Smith, Stan T. Kolaczkowski, and Sean P. Rigby
Catalysis and Reaction Engineering Group, Dept. of Chemical Engineering, University of Bath,
Claverton Down, Bath, BA2 7AY, U.K.

John A. Chudek
Division of Biological Chemistry and Molecular Microbiology, School of Life Sciences,
University of Dundee, Dundee, DD1 4HN, U.K.

DOI 10.1002/aic.10944

Diffusion and reaction within porous media involving condensable vapors are important processes in catalysis, fuel cells, and membrane separations. In this work, 3-D maps of the spatial variation of porosity, pore size and network tortuosity within a porous solid, derived from magnetic resonance images, have been used to construct a structural model for a mesoporous catalyst pellet. Simulations of the kinetic uptake, adsorption and capillary condensation of butane vapor within the porous solid, conducted on the structural model, have successfully predicted experimental measurements of the effects of the onset of capillary condensation on mass transfer rates without the need of the various adjustable parameters prevalent in other models. These findings suggest that accurate mathematical models for both the complex void space of the porous medium, and the mass transport processes taking place within it, have been successfully developed. © 2006 American Institute of Chemical Engineers *AIChE J,* 52: 3278–3289, 2006

Keywords: porous media, condensable vapor, MRI, mass transport, network model

Introduction

Coupled diffusion and reaction within porous media involving condensable vapors are key physical processes for a number of technological systems. Membranes are used to separate condensable from noncondensable vapors.[1] Capillary condensation has been found to accompany heterogeneously catalyzed Fischer-Tropsch[2] reactions, and also industrial hydrotreatment reactions for sulfur or nitrogen removal.[3,4] Condensation within the smaller pores of hydrotreating catalysts has been shown to accelerate coking of the catalyst surface, due to reactions between oxygen from the catalyst and hydrocarbons in the condensate.[3,4] The condensation of water within the pores of the cathode side catalyst in PEM fuel cells significantly affects the performance of the fuel cell because it inhibits the access of oxygen.[5] Capillary condensation of water within the pores of building mortars also affects the rate of carbonation by atmospheric carbon dioxide, and, thus, hardening. Hence, in many systems it is necessary to have a firm understanding of mass transport rates in systems with condensable vapors.

The mathematical modeling of mass transport and reaction accompanied by capillary condensation within porous media has generally made use of pore-bond network models to represent the structure of the void space. Pore-bond networks allow much of the structural complexity of the void space to be incorporated into a model, while still retaining mathematical tractability. In these models, pore sizes, taken from a measured probability density function, are generally assigned to lattice bonds completely at random. In a series of articles, Stubos, Kikkinides and coworkers[1,6-8] studied the permeability of condensable vapors in mesoporous materials using network models. Simulations of adsorption, capillary condensation and mass

---

Correspondence concerning this article should be addressed to S. Rigby at s.p.rigby@bath.ac.uk.

transport were used to determine the effects of material structural parameters and other relevant factors (relative pressure, temperature, and so on.) on vapor permeability. Rajniak and Yang[9] used a Bethe network to represent the porous medium and the effective medium approximation to predict the concentration dependence of the effective diffusivity of a condensable vapor in silica and alumina materials. Wood et al.[3,4] conducted simulations on random pore bond networks of coupled diffusion and reaction processes in hydrotreating catalysts in order to study the effects of network topology (regular vs. random) and pore-structure parameters (mean pore size, standard deviation in pore size, and network connectivity) upon the catalyst effectiveness factor. More recently, potentially more realistic structural models of porous media have been used. Electron microscopy studies[10] have shown that the structures of many porous materials, such as silicas, consist of packings of spheres. Sasloglou et al.[11] have used a realistic random sphere pack model for a compact of microspheres to predict relative permeability curves. However, network models remain very useful, since they can provide explicit analytical expressions of the complex permeability functions, based only on the connectivity and pore-size distribution[12]. Even if a more accurate representation of a pore structure is achieved, such as using a statistical reconstruction method,[13] the next step is often to develop a simpler network model, based on the underlying pore connectivity and pore-size distributions, for which sorption and transport calculations are more mathematically tractable.

In order to use pore bond network models to make *a priori* predictions of a physical process it is necessary to incorporate key descriptors, such as the correct network connectivity of the porous material, prior to simulations. The commonly available methods described in the literature using gas sorption[14] or mercury porosimetry[15] to measure the network connectivity of a porous material almost exclusively assume a completely random pore-bond network. However, imaging studies using microfocus X-ray (MFX)[16] and magnetic resonance imaging (MRI)[17-19] have shown that many mesoporous materials possess macroscopic (~0.01–10 mm) heterogeneities in the spatial distribution of local average porosity (voidage fraction) and pore size. These heterogeneties have been shown to influence both steady-state and transient, liquid-phase, molecular diffusion,[17-19] and the pattern of coke deposition during deactivation of heterogeneous catalysts[20]. Hence, a completely random pore-bond network model for amorphous, porous catalyst and absorbent pellets may be a considerable oversimplification of these highly complex void space structures. It is noted that experimental measurements of tortuosity, made using MRI and PGSE NMR,[18,19,21] for various silica and alumina materials observed to possess macroscopic heterogeneities are significantly lower than would be predicted from random pore bond networks,[22] and pore-size distribution parameters and connectivities determined by gas sorption[14] or mercury porosimetry.[15] In more recent work[23] some researchers have attempted to match nitrogen desorption isotherms for silica particles with simulated isotherms for pore-bond network models with variable lattice size, connectivity *and* spatial distribution of pore size. From this procedure, possible values of lattice size and connectivity, and potential spatial arrangements of pore sizes, were obtained. However, no attempt was made in this work[23] to determine whether the proposed solution was unique. No sensitivity study was carried out to determine all of the possible combinations of the three aforementioned properties of the model that would satisfy the experimental data. Since the approach is indirect, it is quite possible that a large number of alternative combinations of characteristic parameters might be found that also fitted the relatively limited experimental data from primary nitrogen desorption isotherms. However, for many catalyst support and absorbent materials, it is possible to use MRI, in conjunction with relaxation time and diffusion contrast techniques, to directly obtain complete 3-D maps of the spatial variation in local average porosity, pore size and tortuosity (related to pore interconnectivity) within typical pellets.

Recent work[24-26] has shown that in some materials the heterogeneities in the spatial distribution of pore size observed in MR images are not simply due to weak pore-size correlations, resulting in just variations in local averages, but are, in fact, due to very strong correlations in actual pore sizes. The pore structures of many types of mesoporous catalyst support consist of a 3-D "patchwork"of large-scale (~0.01–1 mm) domains. Individual pores within one domain have very similar sizes, but which are significantly different to pores in other domains. Mercury porosimetry experiments have been conducted[27] on micromodels, consisting of pore networks etched in glass where isolated, extended domains of larger pores occur within a continuous network of smaller pores. These experiments have suggested that residual mercury entrapment in this type of system arises from the "snap-off" phenomenon, where the continuity of the mercury mensicus is broken, occurring at the boundaries of larger scale heterogeneities in the spatial distribution of pore size. For some amorphous, catalyst support materials it has been found that the mercury entrapment that arises for whole pellet (~1–10 mm) samples does not occur for fragmented samples (with particle sizes of ~10–100 μm)[24]. In such materials transparent to visible light, microscopy[25] has revealed that the entrapped mercury is confined to particular macroscopic domains that are completely surrounded by clear regions with no entrapped mercury, rather than being homogeneously distributed across the whole pellet, as might be expected for a completely random structure. Integrated gas sorption experiments demonstrated[26] that the entrapped mercury was confined solely to the largest pores in the material. Hence, in the light of the glass micromodel experiments described earlier, it was concluded that the pore structure of the catalyst support pellets consisted of macroscopic domains with segregated pore sizes. Therefore, for these types of materials, MRI is able to directly provide a map of the spatial distribution of particular pore sizes.

In previous work,[28] a model for the pore structure of the sol-gel silica material also studied in this work was constructed using MR spin density and spin-spin relaxation time (T_2) weighted images. Simulations of mercury intrusion and extrusion on the model were found to accurately predict the point of onset of structural hysteresis and the level of residual mercury entrapped at the end of the experiment. The model assumed that the mass transport processes in porosimetry were dominated by the macroscopic (~0.01–10 mm) scale structural heterogeneity evident in the MR images. These findings validated the structural model and the mechanisms of mercury intrusion, extrusion and entrapment used in the simulations, and, thereby, confirmed the nature and importance of the macroscopic structural heterogeneities.

It is the purpose of the work described here to use MRI to construct a more physically representative structural model of amorphous, mesoporous catalyst support pellets than is possible with a random pore-bond network and indirect characterization techniques. This model will be used to obtain *a priori* predictions of the uptake of condensable vapors in the capillary condensation regime without the need for adjustable parameters, such as pore connectivity. In addition, the accurate predictions emerging from a model encourage the belief that a physically realistic mathematical description of the processes taking place has been obtained.

Theory

Construction of structural models

The structural models used in this work are constructed directly from ^{1}H NMR images of pellets fully imbibed with water. NMR imaging using a spin-spin relaxation time contrast preconditioning sequence produces a spin density map and a spin-spin relaxation time map. The pixel intensity in a spin density map is directly proportional to the number of relevant nuclei within the probe water molecules contained in the pixel volume, and, thus, is also proportional to the porosity in that pixel volume. The value of T_2 in each of the pixels of the image may be converted to a pore surface area to volume ratio by the adoption of a relaxation model. For a liquid imbibed in a pore space the relaxation rate is enhanced. This is due to the interactions between the thin layer of liquid at the interface with the solid matrix increasing the relaxation rate. There is also diffusional exchange between the surface-affected layer and the remainder (bulk) of the liquid in the rest of the pore. In the case, as here, where the pores are several orders of magnitude smaller than the rms displacement of the probe water molecules during the course of the experiment, the "two-fraction fast exchange" model of Brownstein and Tarr[29] can be used. The measured value of T_2 is given by

$$\frac{1}{T_2} = (1 - \lambda S_V)\frac{1}{T_{2B}} + \lambda S_V \frac{1}{T_{2S}} \tag{1}$$

where the subscripts S and B refer to the surface layer and bulk fluid, respectively, λ is the thickness of the surface affected layer, and S_V is the pore surface area to volume ratio. In general $T_{2B} \gg T_{2S}$ and, thus, S_V is given, approximately, by

$$S_V \approx \frac{T_{2S}}{\lambda}\frac{1}{T_2} \tag{2}$$

and where S_V would be equal to $2/r$ for a cylindrical pore of radius r. Hence, T_2 is proportional to characteristic pore size.

The value of the relaxation parameter λ/T_{2S} was calibrated using independent measurements of the specific surface area and specific pore volume of the material. The overall average value of T_2 for the material under study was obtained from 3-D T_2 maps of several pellets taken from the same batch. The specific surface area was obtained by fitting the fractal BET equation to data for butane adsorption on the sample, as this method has been shown to give accurate values in previous work.[30] The specific pore volume was obtained by averaging the data for several samples from the same batch obtained using helium-mercury pycnometry. The value of λ/T_{2S} was then calculated using Eq. 2. The spin density for a given pellet was calibrated using the value of the voidage fraction obtained using helium-mercury pycnometry. Hence, the individual values of T_2 and voidage fraction could be calculated for each pixel in an image.

A map of liquid self-diffusivities within a pellet for the same pixel locations as with the T_2 images was obtained by preconditioning the spins with a stimulated pulsed-gradient spin-echo (PGSE) pulse sequence. To obtain the image, the signal intensity S from a pixel i is fitted to the following expression appropriate to the PGSE preconditioning sequence

$$S(i, \delta) \propto \exp[-D(i)\gamma^2 g^2 \delta^2(\Delta - \delta/3)], \tag{3}$$

where $D(i)$ is the value of diffusivity assigned to pixel i, γ is the gyromagnetic ratio, g is the pulsed gradient strength in G.cm^{-1}, δ is the duration of the pulsed gradient, and Δ is the diffusion time. The value of diffusivity measured by PGSE NMR is equal to D_A/τ, where D_A is the free molecular self-diffusivity of the probe fluid (water) and τ is the pore space tortuosity over the length-scale probed during the experiment.[18]

Characterization of the spatial geometric arrangement of a model structure

The T_2 maps obtained using MRI have been analyzed using the fluctuation auto-correlation function $C(s)$, which measures the degree of correlation between $f(x_n)$ values at successive data points. Explicitly, defining δf_n as

$$\delta f_n = f(x_n) - \langle f \rangle \tag{4}$$

then

$$C(s) = \frac{\langle \delta f_n \delta f_{n+s} \rangle}{\langle \delta f_n^2 \rangle} \tag{5}$$

where the averages denoted by the brackets $\langle\ \rangle$ are over the data set $\{x_n\}$. In the context of the images $f(x_n)$ is the characteristic T_2 value in image pixel x_n. For Eq. 5 successive annular shells at a distance s from each pixel are considered for each pixel in turn. The characteristic values of this function are the value of $C(s=1)$ and the value of s when $C(s)=0$. The first value characterizes the degree of correlation, while the second value is known as the correlation length (ξ), and characterizes the linear extent of that correlation.

Mass transport within the structural model

In the capillary condensation regime of the adsorption isotherm the condensable component could be potentially present in one of three phases. In pores within which capillary condensation is yet to occur, and due to the low-mean pressures, mass flux potentially occurs both via the gas-phase component in the free-pore space by Knudsen regime diffusion, and via the adsorbed molecules moving along the pore wall surface. In pores in which capillary condensation has taken place, viscous flow of the condensate can occur.

Zalc et al.[31] have shown, using tracer diffusion simulations within random packing pore structures, that tortuosity factors are independent of diffusion mechanism when an equivalent Knudsen diffusivity is defined in a particular way. Their approach was based on that of Derjagin[32], as later extended by Levitz[33], and leads to an expression for Knudsen diffusivity that captures the statistics of the length-scale distribution, as well as the nature of the redirecting collisions

$$D' = \frac{1}{3}\langle l_p\rangle\langle \nu\rangle\left[\frac{\langle l_p^2\rangle}{2\langle l_p\rangle^2} - \beta\right] \tag{6}$$

$<l_p>$ is the number averaged path length, and is estimated, from simple geometric arguments, to be

$$\langle l_p\rangle = \frac{4\varepsilon}{S_V} \tag{7}$$

where ε is the voidage fraction. Zalc et al.[31] suggest that the ratio $<l_p^2>/2<l_p>^2$ has a value not significantly different to unity for any void fraction. In addition, Zalc et al.[31] showed that the correction term β, related to the statistics of tracer redirections, is generally very similar to the Deraguin[32] limiting value of 0.3077 over a wide range of voidage fractions. $<\nu>$ is the gas mean molecular velocity given by

$$\langle \nu\rangle = \left(\frac{8}{\pi}\frac{RT}{M}\right)^{0.5}, \tag{8}$$

where M is the relative atomic mass, R is the gas constant, and T is the absolute temperature. The local values of the parameters required to estimate the value of $<l_p>$ for a particular region of the void space of a catalyst pellet may be obtained from the equivalent pixels in MRI spin density (which probe voidage fraction) and T_2 (which probe S_V) maps. Hence, for a given region of pore space, the local Knudsen diffusivity can be estimated. Where changes occur in the values of voidage fraction, and S_V due to surface adsorbed phase this can be taken into account in Eq. 6, if the thickness of the adsorbed layer is known (for example, calculated from an isotherm).

In addition to Knudsen diffusion in the void space, mass transport in pores in which adsorption, but not capillary condensation, has occurred can also potentially occur by surface diffusion. In the formulation suggested by Kainourgiakis et al.[7], developed in terms of spreading pressure and a constant surface flow resistance coefficient C_R, the mass flow rate is given by:

$$J_S = \frac{2\pi r\chi^2 RT}{P_m C_R A^2}\frac{\Delta P_g}{l}, \tag{9}$$

where P_m is the mean pressure in a pore bond, A is the specific surface area of the medium, χ represents the amount of fluid sorbed per unit mass of solid, ΔP_g is the change in gas pressure down a pore, l is the length of a pore bond, and r is the radius of the pore. It will be shown below that the surface diffusion mechanism is not important in the particular adsorbate-adsorbent system studied here.

Following multilayer adsorption on the pore wall, capillary condensation occurs at high enough pressures, as determined by the modified form of the Kelvin equation:

$$\frac{P}{P_0} = \exp\left[\frac{\sigma\cos\theta}{\rho_l RT(r - t_m)}\right], \tag{10}$$

where P_0 is the saturation pressure, σ is the surface tension, θ is the contact angle, and t_m is the thickness of the multilayer film. In pores in which capillary condensation has occurred the viscous condensate flux is assumed to obey Poiseuille's equation recast in terms of gas pressure and modified to include an enhancement factor $(\rho_l RT/MP_m)$, which is physically attributed to capillary pressure gradients.[7] An additional driving force occurs due to the difference in the curvatures of the menisci that are formed between nodes and pore bonds filled with condensate. This capillary action is gradually diminished as the mean pressure increases for a given bond because the menisci begin to flatten as the pressure is raised above the particular Kelvin equilibrium condition. This particular effect is taken into account by multiplying the enhancement factor by the term $(r - t_m)^2/r^2$, as suggested by Lee and Hwang[34], such that the constant of proportionality D_c, between the mass-transfer flux down an individual pore (in mol.m^{-2}.s^{-1}), and the gas-phase concentration gradient down the pore is then given by

$$D_c = \frac{r^2\rho_l}{8\eta_l}\left[1 + \frac{(r - t_m)^2}{r^2}\frac{\rho_l RT}{MP_m}\right]\frac{RT}{M}, \tag{11}$$

where η_l is the viscosity of the liquid condensate, and D_c has the same units as diffusivity.

Equations 6 and 11 give the "conductance" of a particular pore bond under different conditions. The values of these conductances may then be used in the appropriate set of Kirchoff equations to solve for the overall conductance of the pore-bond network. Alternatively, for mass transport within a porous medium an effective conductance (diffusivity) D_e may be defined[31] to allow for the restricted cross-sectional area available for mass transport, and the longer and less direct connecting paths, imposed by obstacles (that is, solid phase) within porous solids relative to that for a reference conductance (diffusivity), D_r, such that

$$D_e = \frac{\varepsilon D_r}{\tau}. \tag{12}$$

For example, in a region of void space where pores only have multilayer adsorption and no surface transport D_r would be given by Eq. 6. Whereas, in a region of pore space where capillary condensation had occurred, D_r would be given by Eq. 11. The tortuosity factor is supposed[31] to be solely a function of the geometry of a particular region of void space, and thus independent of mass-transport mechanism (Knudsen diffusion or capillary flow). As mentioned previously, Zalc et al[31]. have shown that tortuosity factors are independent of diffusion mechanism when an equivalent Knudsen diffusivity is defined in the correct way. As also described earlier, the specific tortuosity factor for a particular region of void space can be obtained using MRI preconditioned with a PGSE NMR pulse sequence. The voidage fraction in Eq. 12 can be obtained from the MRI spin density map. Hence, once the state of the condensable vapor in a particular region of void space is known, the effective conductance (diffusivity) for that region can then be calculated using the values of ε, S_V and τ obtained for the corresponding pixel (voxel) in the MRI spin density, T_2 and PGSE maps, respectively, of these parameters.

To a first approximation, a macroscopically heterogeneous porous medium, in which all of the pores in some isolated regions have filled with capillary condensate, can be considered as a two-phase system. One phase corresponds to those regions of the sample in which capillary condensation has occurred, and the other corresponds to those regions where pores are yet to be filled with condensate. Maxwell (cited in Crank[35]) showed that in a two (diffusion) phase system consisting of a suspension of spheres of one phase a, so sparsely distributed in a continuum of the second phase b, such that any interaction between them is negligible, the effective-diffusion coefficient of the composite medium D_w, can be written in the form

$$\frac{D_w - D_b}{D_w + 2D_b} = \nu_a \frac{D_a - D_b}{D_a + 2D_b}, \tag{13}$$

where ν_a is the volume fraction of the dispersed phase. The coefficient D_w is the diffusion coefficient of a hypothetical homogeneous medium exhibiting the same steady-state behavior as the two-phase composite.

When diffusion within a porous solid is accompanied by adsorption, a simple mass balance shows that the usual diffusion equation (here for a sphere) must be modified[35] to allow for this

$$\frac{\partial C}{\partial t} = \frac{D}{(H+1)}\left[\frac{\partial^2 C}{\partial r^2} + \frac{2}{r}\frac{\partial C}{\partial r}\right], \tag{14}$$

where H is the constant of proportionality between the concentrations of the adsorbed phase and the freely diffusing phase. If there is a linear relationship between the concentrations of the surface adsorbed phase and the freely diffusing phase then solutions of the diffusion with adsorption problem, for given initial and boundary conditions, are the same as for the corresponding problem in simple diffusion except that the modified-diffusion coefficient $D/(H+1)$ is used. From standard results[35] involving diffusion within a sphere, following a step increase in external concentration, the total amount of diffusing substance entering the sphere in time t is given by

$$\frac{M(t)}{M(\infty)} = 1 - \frac{6}{\pi^2}\sum_{n=1}^{\infty}\left(\frac{1}{n^2}\right)\exp(-Dn^2\pi^2 t/a^2) \tag{15}$$

where $M(\infty)$ is the equilibrium uptake, D is the (constant) effective diffusion coefficient, and a is the sphere radius. In addition, at later times, (strictly) when the fraction of the mass uptake is > 0.5, Eq 5 can be approximated by the so-called linear driving force (LDF) model and uptake data fitted to the expression

$$\frac{M(t)}{M(\infty)} = 1 - \exp(-kt). \tag{16}$$

where k is a mass-transfer coefficient, equivalent to $15D/a^2$.[36] The uptake method of measuring mass transfer is similar to that used in some previous studies.[9]

Experimental

The material studied in this work is a batch of sol-gel silica spheres, denoted G2, with a typical pellet diameter of ~3 mm, and a nitrogen BET surface area of ~99 $m^2.g^{-1}$. The voidage fraction and specific pore volume, obtained from helium-mercury pycnometry, were 0.69 and 1.07 $cc.g^{-1}$, respectively.

MRI

Samples were prepared by impregnation with de-ionized water under ambient conditions for 24 h. Previous work[17] has shown that this technique leads to complete pore filling. The values of the specific pore volume obtained independently from the ultimate intruded mercury volume and gravimetrically following water impregnation, have been found[28] to be identical, within experimental error. This finding suggests that mercury and water probe the same void space features. MRI experiments were carried out on a Bruker AVANCE NMR System with a static field strength of 7.05 T, yielding a resonance frequency of 300.05 MHz. All samples were placed within a 10 mm Birdcage coil. Spin-spin relaxation time (T_2), and spin-density maps (which probe porosity) were acquired together using the Bruker sequence "*m_msme*", and employed 90° selective and 180° nonselective pulses. A T_2 preconditioned imaging sequence with an echo time of 7 ms was used. 3-D images were acquired using the "*m_se3d*" sequence. The number of scans was typically 240. Data acquisition, initial data transformation, two and three-dimensional data processing, and workup was handled on an SGI O2 5000 workstation, running the Paravision© suite of software (Bruker Analitische Messtechnik Gmbh, Karlsruhe, Germany). The in-plane pixel resolution was 40 μm, and the slice thickness was 250 μm. 3-D spin-echo data was subsequently worked up using AMIRA software. An examination of both simple spin echo and gradient reversal images gave identical results suggesting that images probe pore structure and not simply susceptibility effects. Diffusion-weighted images were acquired using the Bruker PGSE pre-conditioning sequence "*m_diffuse*".

Butane sorption kinetics

Butane sorption experiments were performed on a Hiden intelligent gravimetric analyzer (IGA). In order to obtain an acceptable level of signal-to-noise ratio in the data, the sample generally consisted of 3-4 pellets. The sample was loaded into the IGA and the reactor chamber sealed tightly. The sample was then evacuated to vacuum and heated to 250°C for 24 h. Once completed, the reactor chamber was allowed to cool down to room-temperature. A water jacket was placed around the chamber, and the water bath was set to 0°C. Once the temperature was set to 0°C, the isothermal analysis was performed in the relative pressure region of 0.004 to 1.00 p/p_0. The experiment was all software-controlled, and once completed,

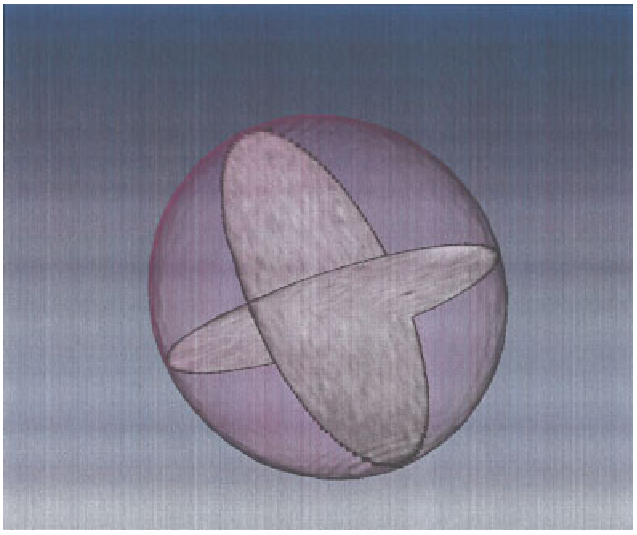

Figure 1. T_2 images of perpendicular 2-D slices through the center of a pellet from batch G2.

The pixel resolution is 40 μm and the slice thickness is 250 μm. [Color figure can be viewed in the online issue, which is available at www.interscience.wiley.com.]

the data values of the adsorption, BET surface area and kinetic data of adsorption were available for analysis. The density and viscosity of liquid butane at 0 °C were taken as 601.863 kg.m^{-3} and 0.21 × 10^{-3} N.s.m^{-2}, respectively.

Results and Discussion

MR Image analysis

Figure 1 shows examples of two T_2-contrasted images of different slices through the center of a spherical pellet from batch G2. The typical value of T_2 for a sample from batch G2 was ~27 ms. This batch was chosen because of its relatively high value of T_2 which allows a higher signal-to-noise ratio to be achieved for a given number of scans. Separate images were obtained of each of the slices in the stack from the top to the bottom of an individual pellet sample taken from batch G2. The individual T_2-contrasted images of slices through pellets taken from batch G2 were analyzed using the auto-correlation function. The variations of the values of $C(s=1)$ and ξ with position within the pellet, for images taken of different slices through a sample of a typical pellet taken from batch G2, are shown in Figure 2. It can be seen that the values of both parameters of the correlation function peak within the central region of the pellet. As shown in Figure 3, this is the result that would be expected if the distribution of T_2 through the pellet possessed some spherical symmetry arising from a correlated structure. It is supposed that the pellet consists of a structure where higher T_2 values, say, are more concentrated toward the center of the sphere and decrease in concentration in weakly-defined bands located progressively further from the center of the pellet. If a 2-D slice MR image were taken of this structure, such that the plane of the image passed through the central zone of the pellet, then, as shown in Figure 3, the image would slice through several different bands and would detect the correlation in T_2 values. Hence, the correlation function would show a relatively high-value of $C(s)$ at shorter distances (corresponding to one pixel). However, if the plane of the 2-D MR image were taken closer to the top ("pole") of the pellet, then it would slice through only one or two bands. The T_2 values within one particular band are envisaged to be closer together than those in different bands, and, hence, the image taken nearer the top of the image would be relatively more dominated by the (unavoidable) noise in the image. Hence, the correlation function would be of a form closer to that expected for a completely random arrangement of pixel intensities (a horizontal line along $C(s) = 0$). The experimental data shown in Figure 2 is consistent with this scenario. Therefore, it is proposed that the structure of pellets from batch G2 has some similarities to the type of structure shown in Figure 3, and possesses some sort of spherical symmetry. Hence, it is reasonable, in this case, to use a 2-D model, constructed from a single central MR image, for the

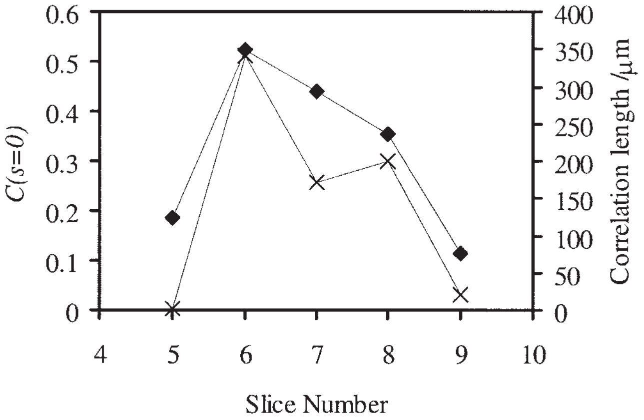

Figure 2. Variation with position of the correlation length (◆) and degree of correlation (x) for T_2 maps of parallel slices of a pellet from batch G2.

The central region of the pellet corresponds to slice 6.

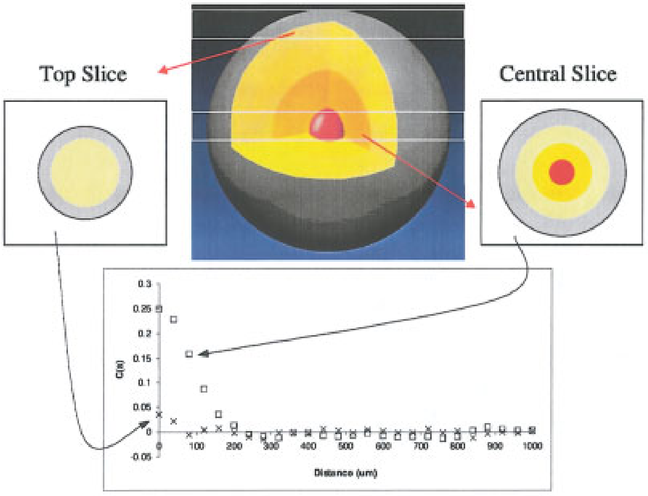

Figure 3. Expected variation of the form of the correlation function with the position of the T_2 image slice if the pellet possessed a spherically symmetric spatial distribution of T_2.

[Color figure can be viewed in the online issue, which is available at www.interscience.wiley.com.]

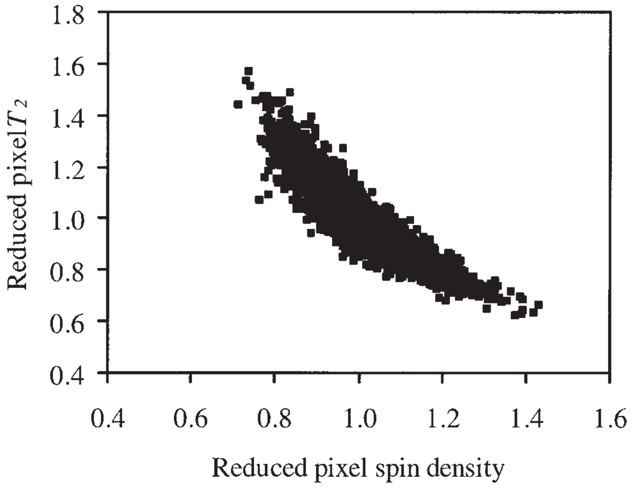

Figure 4. Plot of the reduced spin density against the corresponding value of reduced T_2 for the same pixel location for all the pixels in a typical set of spin density and T_2 images for a central slice through a pellet from batch G2.

The parameters have been reduced by dividing by the relevant mean value within the image.

structure of pellet G2. Figure 4 shows a plot of the value of (reduced) T_2 against the corresponding value of (reduced) spin density for each pixel location in a set of images of an equatorial plane of a pellet taken from batch G2. It can be seen that there is a marked inverse correlation between spin density (corresponding to porosity) and T_2 (corresponding to pore size). Hence, regions of void space containing larger pores tend to have lower overall porosity (voidage fraction). The PGSE NMR (diffusion) maps of pellets from batch G2 revealed no statistically significant variability in tortuosity across the pellet (not shown). The typical tortuosity in pellets from batch G2 is 1.65. This finding is consistent with nonspatially resolved PGSE NMR studies[21] which suggested the log-attenuation plots were highly linear, and that the apparent diffusivity did not change with variations in diffusion time, such that the length-scales probed were 10–39 μm (that is, of the order of the in-plane pixel resolution). Hence, it can be concluded that there is no correlation between where capillary condensation is likely to initially occur and tortuosity.

Modeling of butane adsorption kinetics

Figure 5 shows a typical set of sorption isotherms obtained for butane on G2 at 0 °C. It can be seen that the initial part of the adsorption isotherm is linear, but that it deviates significantly from linearity at relative pressures exceeding ~0.75–0.8. In this high-relative pressure region, where the adsorption isotherm deviates from its initial linearity, the desorption isotherm exhibits hysteresis, whereas the hysteresis loop closes when the desorption reaches the more linear part of the adsorption isotherm. The presence of hysteresis suggests that the deviation from the initial linearity in the isotherm is associated with the onset of capillary condensation. Thus, the initial linear part of the isotherm corresponds to a Henry's law-like region of multilayer buildup. As stated earlier, it is the purpose of this work to predict how the onset of capillary condensation affects mass transport in this system.

Butane adsorption isotherms, and associated uptake kinetics, were obtained for a number of different samples taken from batch G2 at 0 °C. The isotherms were analyzed, using a fractal BET equation, to obtain the BET surface area, as described in earlier work[30], and the values are given in Table 1. The initial linear part of the butane adsorption isotherms were fitted to a straight line using regression analysis. An example of such a fit for sample 1 from batch G2 is shown in Figure 6. The fitted straight line was then extrapolated to the region of relative pressure in which capillary condensation was also occurring in order to deconvolve the fraction of the total amount of adsorbed phase associated with just the multilayer film in that region. The difference between the measured total uptake and the extrapolated Henry's law line was considered to correspond to the amount of adsorbed phase present as condensate in the core zones of pores where capillary condensation was occurring. The (statistical) thickness of the multilayer film (known as the *t*-layer), t_m, was obtained by dividing the volume of adsorbed butane (considered as liquid phase at 0 °C) by the BET surface area.

As mentioned previously, the structural model used to represent the pore structure of batch G2 was constructed from spin density, T_2, and diffusion-weighted magnetic resonance images of "equatorial" slices taken through pellets from batch G2. Since, as demonstrated earlier, the pellets possess spherical symmetry, and the correlation length is smaller than the pellet size, then a single 2-D-slice model was considered sufficient to represent the material. The model consisted of a grid of sites which each corresponded to pixels in the images. Each individual model site thus had its own particular values of spin density, T_2, and tortuosity associated with it. From the spin density and T_2 values the voidage fraction and pore radius (for an equivalent cylindrical pore) could be determined for each

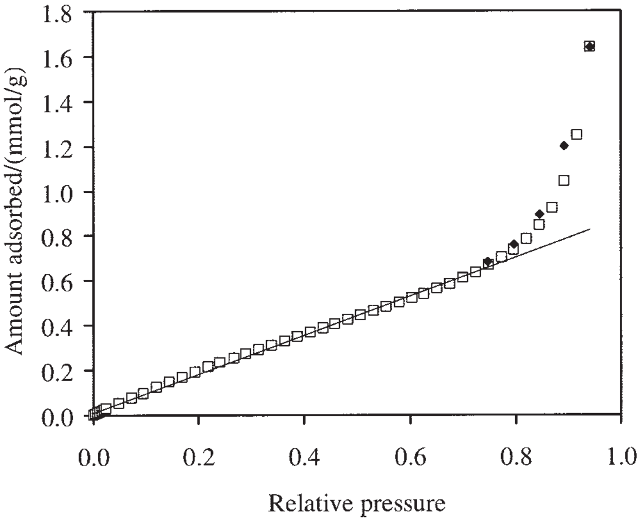

Figure 5. Butane adsorption (□) and desorption (◆) isotherms obtained at 0 °C on a sample from batch G2.

The straight line shown is a linear regression fit to the initial part of the isotherm. The lower desorption points following closure of the hysteresis loop have been omitted for clarity.

Table 1. Comparison of Experimental Measurements and Theoretical Predictions of the Mass-Transfer Coefficients for Butane in Various Samples from Batch G2

Sample	BET Surface Area/ ($m^2 \cdot g^{-1}$)	Relative Pressure of Reference Point Used in Multilayer Region	Relative Pressure of Predicted Point in Capillary Condensation Region	Predicted Ratio of Mass-Transfer Coefficients, Excluding Capillary Flow	Predicted Ratio of Mass-Transfer Coefficients, Including Capillary Flow	Experimentally Measured Ratio of Mass-Transfer Coefficients
1	181.3	0.773	0.918	0.1466 ± 0.0002	0.1718 ± 0.0002	0.173 ± 0.004
			0.942	0.0714 ± 0.0002	0.0970 ± 0.0002	0.097 ± 0.002
2	157.7	0.773	0.918	0.0894 ± 0.0002	0.1103 ± 0.0002	0.133 ± 0.001
3	182.7	0.749	0.918	0.1308 ± 0.0002	0.1488 ± 0.0002	0.144 ± 0.001
			0.942	0.0647 ± 0.0002	0.0828 ± 0.0002	0.08375 ± 0.00001

The quoted errors are one standard error.

site, as described earlier. It was also considered that the total spin density in the model corresponded to the specific volume of the whole sample of real material, and that the total pore surface area in the model corresponded to the BET surface area of the real material. Hence, representative portions of the specific volume and specific surface area could be allocated to each individual model site. From these values the pore volume in a given model site occupied by the multilayer film at any point in the isotherm could then be determined. For isotherm points within the capillary condensation region the model sites considered full of capillary condensate at that pressure could also be determined. The algorithm to do this is as follows. The model sites were listed in order of increasing T_2 (and, thus, characteristic pore size). Model sites were then progressively filled up with capillary condensate (starting with the smallest pore sizes) until the sum of pore-core volumes in the completely filled model sites (that is, excluding the contribution from the multilayer film) equalled the total volume of core condensed phase determined from the difference between the experimental adsorption isotherm and the fitted Henry's law line. An example of a typical visualisation map of the predicted spatial distribution of condensed phase is shown in Figure 7. It can be seen that the pixels predicted to contain pores filled with capillary condensate are typically isolated, or in very small groups. It was, thus, concluded that it is reasonable to use the Maxwell model (Eq. 13) in order to predict overall diffusivity for low levels of capillary condensation.

Preliminary finite difference calculations suggested that, in the purely Knudsen diffusion regime, the additional tortuosity introduced by the hetereogeneity in the spatial distribution of porosity and pore size was negligible in comparison to the effects of capillary condensation. Hence, in subsequent diffusion simulations, the regions of the pellet in which capillary condensation does not arise will be considered as a single diffusional phase. For a given pressure point in the isotherm, the Knudsen diffusivity for each site in the model was calculated using Eqs. 6 and 7. For isotherm points in the capillary condensation region, in the model sites in which capillary condensation was predicted to occur, the capillary flow parameter was calculated using Eq 11. The apparent effective diffusivity for these regions was then calculated using Eq. 12. For a particular pressure point in the capillary condensation region of

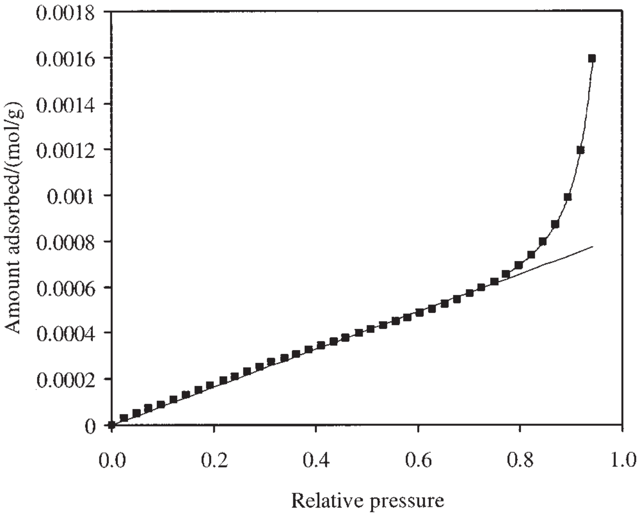

Figure 6. Butane adsorption (■) isotherm obtained at 0 °C on sample 1 (Table 1) from batch G2.

Also shown are a fit of points for relative pressures up to 0.75 to Henry's Law ($y = 8.199 \times 10^{-4}x$, $R^2 = 0.9973$), and a 6th order polynomial fit ($y = 93.21x^6 - 459.9x^5 + 945.8x^4 - 1038x^3 + 640.3x^2 - 210.8x + 28.91$, $R^2 = 1.000$) to points with relative pressures above 0.75.

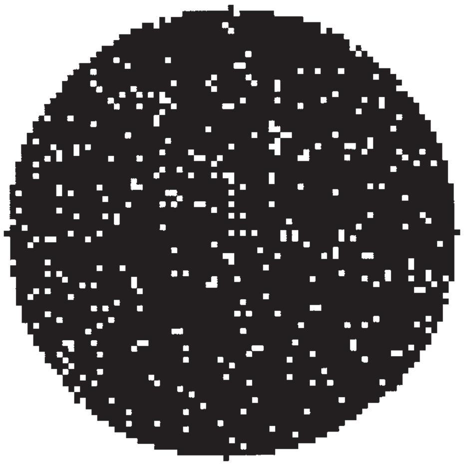

Figure 7. Visualization of the simulated spatial distribution of condensed phase (white) within the equatorial plane of a spherical sol-gel silica G2 pellet from sample 1 during butane adsorption at a relative pressure of 0.942.

The pellet is ~3 mm in diameter.

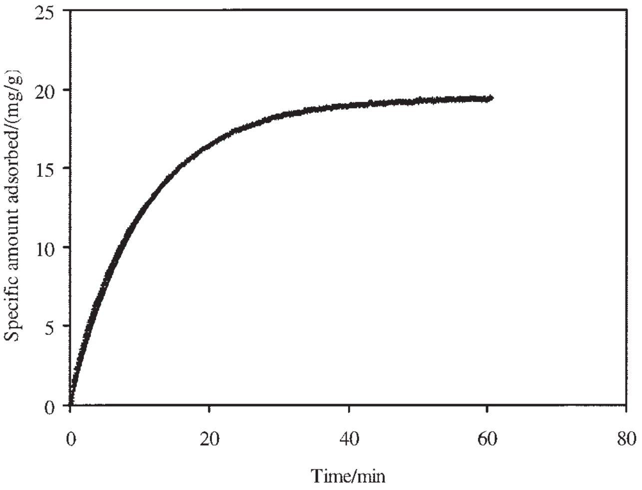

Figure 8. Mass uptake curve (+) for pressure step from relative pressure of 0.918 to 0.941 from the butane adsorption experiment on sample 3 from batch G2.

The solid line shown is a fit of the LDF model to the experimental data for M(t)/M(∞) = 0.816.

the isotherm, the overall apparent diffusivity in the pellet was then calculated as follows. The first model sites filling with capillary condensate up to the first isotherm pressure point showing a deviation from initial linearity were considered one-diffusional phase. The model sites that were not to contain any capillary condensate, even up to the particular higher-pressure point being considered, were taken as the second-diffusional phase. The diffusivity in the second phase was taken as the arithmetic mean of the effective diffusivities for each model site calculated using Eqs. 6, 7 and 12. The volume fraction for the first phase was calculated taking the total number of sites as the sum of the number of sites filled in the first pressure step deviating from the Henry's law line, and all sites that were not filled with capillary condensate up to the ultimate pressure being considered. The overall diffusivity for the first subset of sites was then calculated using Eq. 13. This entire first subset of sites was, thus, then considered as the continuum -diffusion phase in the calculation corresponding to the next highest pressure point. Model sites that were filled with condensate between the first and second capillary condensation region pressure-points were then considered as the second dispersed phase. The overall diffusivity for the second subset of model sites was then calculated using Eq. 13, and this subset then became the continuum for the next pressure-point calculation. This procedure was repeated until the final pressure point being considered was reached. Using this procedure the effect of pore-size variation on the capillary flow rate can be taken into account.

The final prediction for the observed diffusivity at a particular capillary condensation region pressure point was then obtained by dividing the diffusivity, calculated as earlier from Eq. 13, by the slope of the isotherm at that point plus one, as in Eq. 14. The slope of the isotherm at a particular point was obtained by fitting intervals of the raw isotherm data to sixth-order polynomials, and then differentiating the fitted equation to obtain an expression for the variation of slope with pressure. An example of such a fit is shown in Figure 6. In order to clearly demonstrate the effects of capillary condensation on mass transport the model predictions for the ratio of the diffusivities at particular upper points in the capillary condensation region to that of an uppermost pressure point in the multilayer region were obtained. These predictions are shown in Table 1. Since samples for kinetics experiments typically consist of ~3 pellets, while individual pellets are imaged using MRI, the predicted ratios of the mass-transfer coefficients given in Table 1, are sample means for the separate predictions made using several images of different pellets from batch G2.

Comparison of model predictions with experiment

The predictions of the changes in mass transport rates following the onset of capillary condensation have been compared with experimental measurements for butane on G2. The equilibrium adsorption isotherms described above were obtained by making small, stepwise increases in the external pressure of adsorbate, and observing the temporal variation in mass uptake into the sample until equilibrium was reached at each stage. These kinetic data can be used to determine the variation of the mass-transport coefficients with adsorbate uptake. Figure 8 shows an example of a typical uptake curve for a pressure point on a butane adsorption isotherm. The data from the uptake curves was fitted to the two-parameter (*M(∞)* and *k*) LDF model (Eq. 16). It was checked that each isotherm data point had reached equilibrium by ensuring the value of the fitted parameter *M(∞)* from the LDF model agreed with the mass uptake values in the final plateau of the uptake curves. In general, as in Figure 8, when the parameters of the LDF model are derived from the upper part of the uptake curve, it still gives rise to a reasonable fit to the lower part of the curve.

Figure 9 shows the variation of the mass-transport coefficient (MTC), obtained from fitting the LDF model, with amount adsorbed for pressure points in the upper part of the Henry's law region of the typical butane adsorption isotherm for a sample from batch G2 shown in Figure 6. It can be seen that the MTC declines almost linearly with amount adsorbed.

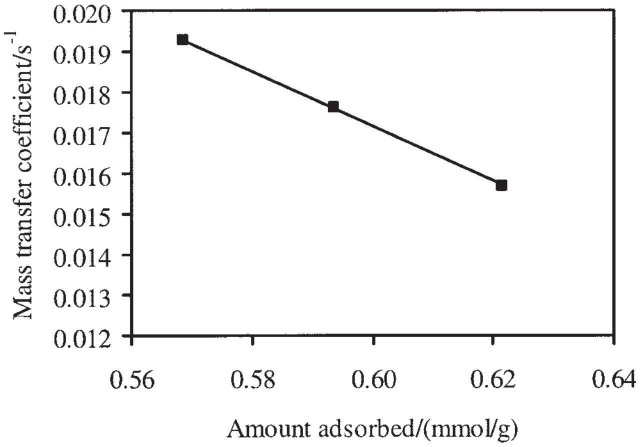

Figure 9. Variation of LDF mass-transfer coefficients with amount adsorbed for uppermost points of Henry's law (multilayer) region of the butane isotherm for sample 1 from batch G2 shown in Figure 6.

Table 2. Variation with Fitted Data Range of the Mass-Transfer Coefficient Obtained from the LDF Model for the Raw Adsorption Uptake Data Shown in Figure 8

Fitted Range of $M(t)/M(\infty)$	Mass Transfer Coefficient, k/min^{-1}
0.583-1	0.094804
0.700-1	0.093978
0.817-1	0.093433
0.933-1	0.093448

This decrease is what would be expected if mass transport is generally occurring via the Knudsen diffusion mechanism, as the core void volume in the pores decreases due to increased multilayer buildup with rising pressure. However, from Eq. 9, it is the opposite trend to what would be expected if surface diffusion was the predominant, or even a significant, contribution to mass transport. Hence, it is suggested that, prior to capillary condensation, mass transport of butane occurs by Knudsen-pore diffusion.

The LDF model was fitted to uptake curves for all pressure points in the isotherm, including the capillary condensation region of the isotherms. Normally, as many data points as possible are used in the fitting procedure to reduce random error, but, in the case of the capillary condensation region, the limit in the value of the mass-transfer coefficient, as the mass uptake tended to equilibrium, was obtained. This was to alleviate potential sources of systematic error (described later) that are significant in the capillary condensation region. An example, for the pressure uptake step shown in Figure 8, is given in Table 2. From Table 2, it can be seen that, while the value of *k* is relatively insensitive to the fitted data range, it does tend to a limit as *M(∞)* becomes greater than ~0.8. It was supposed this was because this upper region mostly closely corresponds to what had been predicted above with the model. First, the value of *H* determined from the differentiation of the polynomial fit to the upper part of the isotherm strictly only applies at a particular pressure point. Thus, the assumption of a linear relationship between the concentrations of the adsorbate in the gas phase and adsorbed phase only applies over a limited pressure range for the curved upper part of the isotherm. Ideally, an isotherm would be acquired using very tiny pressure steps over which the assumption of linearity would be most accurate, but in order to improve the signal-to-noise ratio in the data larger pressure steps are actually used. However, if only the upper part of the kinetic uptake curve is fitted to the LDF, then the value of *H* corresponding to the upper part of the pressure step is appropriate to use in making mass-transport predictions. Second, Eq. 13 was, strictly, derived for steady-state diffusion within a two-phase system. However, in the upper part of the kinetic mass uptake curve the concentration gradient across the pellet is changing relatively little, and, thus, most closely approximates steady-state conditions. Fitting the uppermost part of the uptake curve is also better for experimental reasons. The uppermost part of the curve is most far removed from the potential perturbations caused by the fact that a perfect step increase in pressure is not physically realizable. In addition, the uppermost part of the curve, where relatively little mass is generally being adsorbed over relatively longer periods, is less affected by potential heat transfer effects due to the larger amounts of adsorbate condensing out in the upper part of the isotherm and releasing large amounts of heat of adsorption.

Table 1 shows, for various samples taken from batch G2, the ratios of the mass transport coefficients determined, using the LDF model, for various pressure points at which significant capillary condensation has occurred, to the uppermost pressure points in the multilayer region of the respective isotherms. The ratios were determined using the limiting value for the mass-transfer coefficient for pressure points in the capillary condensation region. It can also be seen from Table 1 that the above model makes good predictions for these values. For comparison purposes, Table 1 also contains predictions of the ratios of the mass-transport coefficients made using a model that neglects the contribution of capillary flow within the pellet. It can be seen that this model makes very poor predictions of this ratio. The observed rate of mass uptake has, thus, been found to be critically dependent on the overall volume fraction of the pellet occupied by regions containing condensed phase, and their particular spatial locations. The exact size of the contribution of capillary flow to the overall mass-transport rate of the condensable vapor is very sensitively determined by the volume fraction in Eq. 13. The specific volume of pores of a given size, where condensation has occurred, may be spatially distributed across the pellet in an infinite number of possible combinations of differing numbers of regions of varying porosity. MRI is able to provide this critical information, as shown in Figures 1 and 4, and, thus, we have been able to successfully predict the rate of uptake of butane adsorbing onto silica in the highly complex capillary condensation regime. In even higher-pressure regions of the butane adsorption isotherm, beyond the capabilities of the apparatus used, the isolated capillary condensation regions observed in lower pressure points may begin to join-up and even form a percolating network which would significantly change mass-transport rates. The onset of this percolation effect in a system that is not homogeneously random could be predicted from the spatial information on heterogeneity obtainable using MRI, and this will be the subject of a future work. Recently MRI has also been used to obtain spatially resolved adsorption isotherms for porous solids.[37] In addition, gas phase MRI[38] has been used to obtain concentration profiles for the transient diffusion of a gas into a porous solid. Hence, further MRI studies could be used to test other predictions of the model reported here, besides overall uptake rates, such as the specific-spatial distribution of condensed phase and the local mass-transfer fluxes in different regions of the pellet.

Due to the relatively narrow relative pressure range considered, and the nature of the particular adsorbate-adsorbent pair studied here, the effects of the spatial arrangement of capillary condensation on transport are dominated by the influence of the macroscopic pore structural heterogeneities detected using MRI. Hence, in this case, a relative simple description of the adsorbed phase, in terms of either adsorbed multilayer, or completely filled void space regions, was sufficient. However, for other combinations of adsorbate and adsorbent, the distribution of adsorbed phase may be much more complex, and involve significantly more heterogeneity, particularly at the pore scale, as well as the macroscopic scale. Hence, in general, MRI can be viewed as an additional technique which can be combined with other complementary methods, such as helium relative permeability[8], and contrast matching small-angle neutron scattering,[39] which provides information on the pore scale distribution of the condensate, to study transport with accompanying capillary condensation.

Conclusions

Magnetic resonance images of the spatial distributions of spin density, spin-spin relaxation time, and self-diffusivity, across a mesoporous, sol-gel silica pellet have been used to construct a structural model for the pellet incorporating spatial variation in voidage fraction, pore size, and tortuosity. This structural representation has been used, in conjunction with a mathematical model for mass transport of a condensable vapor, to make successful predictions of the significant effect of capillary condensation on mass transport of butane within the silica pellet. These findings confirm that the structural data used contains sufficient information to completely represent the pore structure of the material, and the mathematical model provides a good description of the physical processes taking place within the pellet.

Acknowledgments

SPR, STK and MJW-S thank the EPSRC for financial support (under grant no. GR/R61680/01).

Literature Cited

1. Kainourgiakis ME, Kikkinides ES, Stubos AK, Kanellopoulos NK. Adsorption-desorption gas relative permeability through mesoporous media- network modelling and percolation theory. *Chem Eng Sci.* 1998;53:2353-2364.
2. Xu B, Fan Y., Zhang Y, Tsubaki N. Pore diffusion simulation model of bimodal catalyst for Fischer-Tropsch synthesis. *AIChE J.* 2005;51:2068-2076.
3. Wood J, Gladden LF. Modelling diffusion and reaction accompanied by capillary condensation using three-dimensional pore networks. Part 1. Fickian diffusion and pseudo-first-order reaction kinetics. *Chem Eng Sci.* 2002;57:3033-3045.
4. Wood J, Gladden LF, Keil FJ. Modelling diffusion and reaction accompanied by capillary condensation using three-dimensional pore networks. Part 2. Dusty gas model and general reaction kinetics. *Chem Eng Sci.* 2002;57:3047-3059.
5. Natarajan D, Van Nguyen T. Current distribution in PEM fuel cells. Part 1: Oxygen and fuel flow rate effects. *AIChE J.* 2005;51:2587-2598.
6. Kainourgiakis ME, Stubos AK, Konstantinou ND, Kanellopoulos NK, Milisic V. A network model for the permeability of condensable vapors through mesoporous media. *J Membrane Sci.* 1996;114:215-225.
7. Tzevelekos KP, Kikkinides ES, Stubos AK, Kainourgiakis ME, Kanellopoulos NK. On the possibility of characterising mesoporous materials by permeability measurements of condensable vapours: theory and experiments. *Adv Colloid Interface Sci.* 1998;76-77:373-388.
8. Tzevelekos KP, Romanos GE, Kikkinides ES, Kanellopoulos NK, Kaselouri V. Experimental investigation on separations of condensable from non-condensable vapours using mesoporous membranes. *Micro Mesoporous Mater.* 1999;31:151-162.
9. Rajniak P, Yang RT. Unified network model for diffusion of condensable vapours in porous media. *AIChE J* 1996;42:319-331.
10. Reyes SC, Iglesia E. Effective diffusivities in catalyst pellets- new model porous structures and transport simulation techniques. *J Catal.* 1991;129:457-472.
11. Sasloglou SA, Petrou JK, Kanellopoulos NK, Androutsopoulos GP. Realistic random sphere pack model for the prediction of relative permeability curves. *Micro Mesoporous Mater.* 2001;47:97-103.
12. Petropoulos JH, Petrou JK, Kanellopoulos NK. Explicit relation between relative permeability and structural parameters in stochastic pore networks. *Chem Eng Sci.* 1989;4:2967-2977.
13. Kainourgiakis ME, Steriotis ThA, Kikkinides ES, Romanos G, Stubos AK. Adsorption and diffusion in nanoporous materials from stochastic and process-based reconstruction techniques. *Colloids Surf A: Physicochem Eng Aspects*. 2002;206:321-334.
14. Rigby SP, Watt-Smith MJ, Fletcher RS. Simultaneous determination of the pore-length distribution and pore connectivity for porous catalyst supports using integrated nitrogen sorption and mercury porosimetry. *J Catal* 2004;227:68-76.
15. Portsmouth RL, Gladden LF. Determination of pore connectivity by mercury porosimetry. *Chem Engng Sci.* 1991;46:3023-3036.
16. Rigby SP, Fletcher RS, Raistrick JH, Riley SN. Characterisation of porous solids using a synergistic combination of nitrogen sorption, mercury porosimetry, electron microscopy and micro-focus X-ray imaging techniques. *Phys Chem Chem Phys.* 2002;4:3467-3481.
17. Hollewand MP, Gladden LF. Heterogeneities in structure and diffusion within porous catalyst support pellets observed by NMR imaging. *J Catal.* 1993;144:254-272.
18. Hollewand MP, Gladden LF. Transport heterogeneity in porous pellets-II. NMR imaging studies under transient and steady-state conditions. *Chem Eng Sci.* 1995;50:327-344.
19. Rigby SP, Cheah K-Y, Gladden LF. NMR imaging studies of transport heterogeneity and anisotropic diffusion in porous alumina pellets. *Appl Catal.* 1996;A144:377-388.
20. Cheah K-Y, Chiaranussati N., Hollewand MP, Gladden LF. Coke profiles in deactivated alumina pellets studied by NMR imaging. *Appl Catal.* 1994;115:147-155.
21. Rigby SP, Gladden LF. The use of magnetic resonance images in the simulation of diffusion in porous catalyst support pellets. *J. Catal.* 1998;173:484-489.
22. Hollewand MP, Gladden LF. Modelling of diffusion and reaction in porous catalysts using a three-dimensional network model. *Chem Eng Sci.* 1992;47:1761-1770.
23. Meyers JJ, Nahar S, Ludlow DK, Liapis AI. Determination of pore connectivity and pore size distribution and pore spatial distribution of porous chromatographic particles from nitrogen sorption measurements and pore network modelling theory. *J Chromatogr A* 2001;907:57-71.
24. Rigby SP, Edler KJ. The influence of mercury contact angle, surface tension and retraction mechanism on the interpretation of mercury porosimetry data. *J Colloid Interface Sci.* 2002;250:175-190.
25. Rigby SP, Fletcher RS, Riley, SN. Determination of the cause of mercury entrapment during porosimetry experiments on sol-gel silica catalyst supports. *Appl Catal. A* 2003;247:27-39.
26. Rigby SP, Fletcher RS, Riley SN, Characterisation of porous solids using integrated nitrogen sorption and mercury porosimetry. *Chem Eng Sci.* 2004;59:41-51.
27. Wardlaw NC, McKellar M. Mercury porosimetry and the interpretation of pore geometry in sedimentary rocks and artificial models. *Powder Technol.* 1981;29:127-143.
28. Watt-Smith MJ, Rigby SP, Chudek JA, Fletcher RS, Simulation of nonwetting phase entrapment within porous media using magnetic resonance imaging. *Langmuir* 2006;22:5180-5188.
29. Brownstein KR, Tarr CE. Spin-lattice relaxation in a system governed by diffusion. *J Magn Reson.* 1977;26:17-24.
30. Watt-Smith MJ, Edler KJ, Rigby SP. An experimental study of gas adsorption on fractal surfaces. *Langmuir.* 2005;21:2281-2292.
31. Zalc JM, Reyes SC, Iglesia E. The effects of diffusion mechanism and void structure on transport rates and tortuosity factors in complex porous solids. *Chem Eng Sci.* 2004;59:2947-2960.
32. Deraguin B. Measurement of the specific surface of porous and disperse bodies by their resistance to flow of rarified gases. *Comptes Rendu (Doklady) de l'Academie des Sciences de l'URSS.* 1946;53:623-626.
33. Levitz P. Off-lattice reconstruction of porous media: critical evaluation, geometrical confinement and molecular transport. *Adv Colloid Interface Sci.* 1998;76-77:71-106.
34. Lee KH, Hwang ST. The transport of condensable vapours through a microporous vycor glass membrane. *J Colloid Interface Sci.* 1986;110:544-555.
35. Crank J. *The Mathematics of Diffusion*. Oxford: Clarendon Press; 1975.
36. Sircar S, Hufton JR. Why does the linear driving force model for adsorption kinetics work?. *Adsorption.* 2000;6:137-147.
37. Beyea SD, Caprihan A, Glass SJ, DiGiovanni A. Nondestructive characterization of nanopore microstructure: Spatially resolved

Brunauer-Emmett-Teller isotherms using nuclear magnetic resonance imaging. *J Appl Phys.* 2003;94,935-941.

38. Ramanathan C, Bencsik M. Measuring spatially resolved gas transport and adsorption in coal using MRI. *Magn Reson Imaging.* 2001;19,555-559.
39. Smarsly B, Göltner C, Antonietti M, Ruland W, Hoinkis E. SANS investigation of nitrogen sorption in porous silica. *J Phys Chem. B* 2001;105, 831-840.

Manuscript received Feb. 7, 2006, and revision received Jun. 6, 2006.